Title	Thermodynamic evaluation of the solidification phase of molten core-concrete under estimated Fukushima Daiichi Nuclear Power Plant accident conditions
Author(s)	Kitagaki Toru, Yano Kimihiko, Ogino Hideki, Washiya Tadahiro
Citation	Journal of Nuclear Materials, 486, p.206-215
Text Version	Author's Post-print
URL	https://jopss.jaea.go.jp/search/servlet/search?5057304
DOI	https://doi.org/10.1016/j.jnucmat.2017.01.032
Right	© 2017. This manuscript version is made available under the CC-BY-NC-ND 4.0 license http://creativecommons.org/licenses/by-nc-nd/4.0/

Thermodynamic evaluation of the solidification phase of molten core–concrete under estimated Fukushima Daiichi nuclear power plant accident conditions

Toru Kitagaki [a,*], Kimihiko Yano [a], Hideki Ogino [a], and Tadahiro Washiya [a]

[a] Collaborative Laboratories for Advanced Decommissioning Science, Japan Atomic Energy Agency, 4-33 Muramatsu, Tokai-mura, Ibaraki, 319-1194 Japan

* Corresponding author. Tel.: +81-29-282-1126; fax: +81-29-282-1517.
E-mail address: kitagaki.toru@jaea.go.jp

Abstract

The solidification phases of molten core–concrete under the estimated molten core–concrete interaction (MCCI) conditions in the Fukushima Daiichi Nuclear Power Plant Unit 1 were predicted using the thermodynamic equilibrium calculation tool, FactSage 6.2, and the NUCLEA database in order to contribute toward the 1F decommissioning work and to understand the accident progression via the analytical results for the 1F MCCI products. We showed that most of the U and Zr in the molten core–concrete forms $(U,Zr)O_2$ and $(Zr,U)SiO_4$, and the formation of other phases with these elements is limited. However, the formation of $(Zr,U)SiO_4$ requires a relatively long time because it involves a change in the crystal structure from fcc-$(U,Zr)O_2$ to tet-$(U,Zr)O_2$, followed by the formation of $(Zr,U)SiO_4$ by reaction with SiO_2. Therefore, the formation of $(Zr,U)SiO_4$ is limited under quenching conditions. Other common phases are the oxide phases, $CaAl_2Si_2O_8$, SiO_2, and $CaSiO_3$, and the metallic phases of the Fe–Si and Fe–Ni alloys. The solidification phenomenon of the crust under quenching conditions and that of the molten pool under thermodynamic equilibrium conditions in the 1F MCCI progression are discussed.

1. Introduction

Loss of coolant in a light-water reactor may lead to the formation of a molten core, which is a mixture of molten nuclear fuel and structural materials. When the molten core penetrates the wall of the reactor pressure vessel (RPV), it reacts with the concrete in the primary containment vessel (PCV); this process is referred to as a molten core–concrete interaction (MCCI). During this process, a mixture of products is formed from the molten core–concrete. Several codes for simulating an MCCI have been developed, such as TOLBIAC-ICB, ASTEC/MEDICIS, and COCO; these are used in order to estimate the timing or possibility of damage to the wall of the PCV for reactor safety evaluations [1–3]. Moreover, knowing the

characteristics of the corium and MCCI products is important for decommissioning severely damaged reactors. For example, knowing the mechanical and thermal properties of the corium and MCCI products is necessary to retrieve them from a damaged reactor [4], and knowing their chemical properties is necessary for developing appropriate treatment technology [5]. The characteristics of the debris accumulated in the RPV can be estimated from those of the debris and corium produced by severe-accident experimental programs, such as the Phebus-FP and MASCA projects, at the Three Mile Island Nuclear Power Plant Unit 2 (TMI-2) [6–9]. On the other hand, although MCCI test products have been analyzed at the millimeter and centimeter scale with respect to understanding the MCCI progression [10,11], knowledge of characteristics such as the phase and microstructure of MCCI products at the micrometer scale is limited to information on Chernobyl lava-like fuel-containing materials (LFCM) and corium spreading test materials [12,13]. Moreover, the composition of an LFCM differs from that of an MCCI product generated in a light-water reactor (LWR). Chernobyl's LFCM contains a large amount of carbon, sand, and Pb because the Chernobyl Nuclear Power Plant (NPP) Unit 4 was a graphite-moderated nuclear power reactor and because sand and Pb were dropped into the reactor just after the accident to shield the damaged core.

Thermodynamic equilibrium calculations are one of the tools used to evaluate equilibrium phases under various conditions, and these have been used to calculate the equilibrium phases of an MCCI [14]. Moreover, a thermodynamic database, NUCLEA, which can be coupled with CALPHAD methods, was developed by Thermodata for nuclear engineering applications; this includes elements contained in MCCI products, such as O, U, Zr, Fe, Cr, Ni, Al, Ca, and Si [15]. Thermodynamic calculations based on NUCLEA have been used in the MCCI calculation codes mentioned above to estimate the crust composition as well as the liquidus and solidus temperatures, which depend on the oxide compositions [1]. However, phase changes during the solidification of molten core–concrete were not considered because these studies had different purposes.

In this study, the tendencies of the phase changes during the solidification of molten core–concrete were evaluated. The composition and cooling rate of molten core–concrete have a large impact on the solidification phases. The calculation conditions required to simulate the cooling rate are discussed along with the analytical results for a VULCANO VE-U1 test sample [13], because this is the only available information that shows the differences in the solidification process of molten core–concrete, depending on the cooling rate. In addition, we selected a boiling-water reactor (BWR) as the core material and basaltic concrete as the concrete component in our calculations. This is one of the most common conditions found in Japanese NPPs, including the Fukushima Daiichi NPP (1F). Our results will enable a more

detailed discussion regarding removal of the MCCI products from 1F.

Details of the progression of an accident are important for the verification of severe-accident analysis codes. The phases of the MCCI products allow elucidation of the local oxygen potential and temperature levels during the accident. The detailed phase changes of some characteristic phases as a function of the oxygen potential and temperature are also discussed in the following sections.

2. Calculation conditions

2.1 Calculation tools

FactSage 6.2 and NUCLEA (version 2005-01) were used as a thermodynamic equilibrium calculation code and thermodynamic database, respectively. Although the NUCLEA database is inadequate for evaluating mutual solubility between phases, it appears to be sufficient for understanding the tendencies of the phase changes during the solidification of molten core–concrete. References [15] and [16] refer to the reliability and advancement of FactSage and NUCLEA.

2.2 Selection of cooling rate conditions using VE-U1 test samples

The reported phases and the microstructure of the VE-U1 test product, which was generated in the large-scale MCCI test facility PLINIUS/VULCANO, were evaluated with respect to corium spreading behavior on a ZrO_2 base plate; the results were used in discussing a method for simulating the cooling rate of molten core–concrete materials [13]. The reported conditions are described below.

The composition of the test product was O:U:Zr:Si:Fe:Ca:Mg:Al with a wt% ratio of 25.5:38.7:16.9:9.7:8.8:0.2:0.1:0.1. The experiment was performed under atmospheric pressure. After the corium spreading test, the test products were segregated into three distinct layers according to their different cooling rates. The analyzed phases of each layer are shown in Table 1. The top layer, which was cooled at the most rapid cooling rate of 85–100 K/s, contained $(U,Zr,Fe)O_{2-x}$ and SiO_2. The bulk layer, which was cooled at a mid-level cooling rate of about 10 K/s, contained $(U,Zr,Fe)O_{2-x}$, SiO_2, and $Fe_{1.2}SiO_{3.56}$. The bottom layer, which was cooled at the slowest cooling rate of below 10 K/s, contained UO_2, $(Zr,U)SiO_{4-x}$, SiO_2, and $Fe_{2.2}SiO_{3.76}$.

In the thermodynamic calculation, the composition of the molten materials, maximum temperature, and pressure were defined as input data. The above-mentioned test conditions were used as a reference. The composition of the molten materials was set to be the exact composition of the three-layer composition mentioned above. The maximum temperature was set to 2,500 K, which was higher than the calculated liquidus temperature. The input

pressure for this calculation was 1 atm. Moreover, the Scheil equation was used to simulate the solidification phases under quenching conditions [17].

2.3 Calculation conditions based on the estimated 1F Unit 1 conditions

The phases of the MCCI products at 1F Unit 1 (1F1) were evaluated as examples of MCCI products generated in an actual plant. In the case of the 1F1 accident, it was estimated via the MAAP code that all of the molten core leaked through the bottom of the RPV wall and accumulated on the concrete of the drywell floor [18]. A larger amount of concrete probably reacted with molten corium around the two sump pits in comparison to the rest of the drywell floor because of the low elevation of the two sump pits above the drywell floor. Therefore, the solidification phases of molten core–concrete in the sump pits were estimated in this study.

The composition of the molten corium accumulated in a sump pit before the start of the MCCI was defined on the basis of the composition of the fuel and the structural materials in the RPV, as shown in Table 2 [19]. The composition of the core internals was presumed to be 74 wt% Fe, 18 wt% Cr, and 8 wt% Ni (that of an austenitic stainless steel), and the percentage of Sn in Zircalloy was presumed to be negligible in order to simplify the calculation. Neutron-absorbing materials, such as B_4C, were not considered in this calculation because their mass is relatively low and the majority of B_4C could oxidize to B_2O_3 and then evaporate during the progression of an accident in the RPV and during the MCCI. The changes in the fuel composition due to burnup were not considered in this study.

Molten corium, including metallic phases such as Zr and Fe–Cr–Ni, was partially oxidized throughout the in-core accident progression and the MCCI. The order of oxidation is Zr, Cr, Fe, and Ni, as determined from the standard free energies shown in Figure 2 [20, 21]. Therefore, the oxidized states, UO_2–Zr–Fe−Cr−Ni, UO_2–ZrO_2–Fe−Cr−Ni, and UO_2–ZrO_2–Fe_2O_3−Cr_2O_3−NiO were considered in this work.

The composition of the 1F1 concrete was estimated via the analytical results for Al, Ca, Fe, and Si (shown in Table 3 [22]) for a concrete sample taken from the 1F1 reactor building. The estimated concrete composition was 53.5 wt% SiO_2, 10.9 wt% CaO, 13.2 wt% Al_2O_3, and 5.1 wt% Fe_2O_3, which total 82.7 wt%. Although it is considered that the other phases in the concrete should include H_2O, CO_2, and small amounts of materials such as Mg, we neglected these materials. Instead, the effect of material oxidation by H_2O and CO_2 is considered to cause the oxidation of Zr and Fe–Cr–Ni, as mentioned above. Small amounts of materials have little influence on the phases typically found in concrete. The iron bars used to enhance the strength of the concrete were not considered in this calculation, because these would exist only below the pedestal wall.

The ratios of corium and concrete in an MCCI product depends on the volume of the ablated concrete. The amount of ablated concrete was estimated from the MAAP calculation results [19]. These results show that the ablation length of concrete toward the bottom and in the radial direction in a sump pit is 0.65 m and that the ablated shape of concrete in the top-down view of a sump pit is somewhere between that of a square and a circle (see Figure 1). The volume and weight of the ablated concrete based on these shapes were estimated using the density of typical concrete [23], as shown in Table 4. The calculation conditions are summarized in Table 5. These compositions include less oxidative and excessively oxidative conditions, quenching, and thermodynamic equilibrium conditions.

3. Calculation results

3.1 Selection of cooling rate conditions

The mass fractions of the calculated phases in the bottom layer are shown in Figure 3(a) as a function of temperature. Because the cooling rate was lowest in the bottom layer, we used a thermodynamic equilibrium condition without the Scheil equation (Case 4, Table 1) for this layer. During the cooling process of the molten liquid (1) and (2), the order of solidification is as follows: cubic-$(U,Zr)O_2$ (3), $(Zr,U)SiO_4$ (4), cristobalite (5), Fe_3O_4 (8), and Fe_2SiO_4 (9). $(Zr,U)SiO_4$ is a Zr monoclinic crystal phase containing a higher U concentration than natural minerals; this phase was detected in Chernobyl LFCM [24]. The crystal structure of SiO_2 changes from cristobalite (5) to tridymite (6) and quartz (7). The calculated phase at 1,000 K is shown in Case 4 in Table 1 and compared with the analytical phases. The calculated phases correspond to the actual phases, except for Fe_3O_4. Fe_2SiO_4 is found together with Fe_3O_4 under the slower cooling conditions, while in the test samples only Fe_2SiO_4-type compounds are found. The oxygen potential in the bottom layer was also lower than that under the estimated conditions because Fe_2SiO_4 is formed under reduced oxidation conditions. The detailed reaction of Fe–Si–O is discussed in section 3.4.

In the middle layer (Case 3, Table 1), the actual phases show phase segregation of $(U,Zr,Fe)O_2$ into a U-rich and a Zr-rich phase and an absence of $(Zr,U)SiO_4$, Although the formation behavior of $(Zr,U)SiO_4$ should be discussed on the basis of both crystal growth kinetics and thermodynamic equilibrium, the detailed reaction of $UO_2 - ZrO_2 - SiO_2$ is discussed in section 3.3 on the basis of only thermodynamic equilibrium conditions. The phases simulated under the equilibrium condition without $(Zr,U)SiO_4$ formation (Case 3, Table 1) are in reasonable agreement with the actual phases. Phase segregation of $(U,Zr)O_2$ in the simulated phases is more pronounced than that in the actual phases. The molar fractions of U and Zr in $(U,Zr)O_2$ as a function of temperature are shown in Figure 4. Phase segregation of $(U,Zr)O_2$ proceeded in line with decreasing temperatures. It appears that at

temperatures below ~1,750 K, the cooling rate of the actual phase was too fast to reach thermodynamic equilibrium because the calculated mass fraction of U in $(U,Zr)O_2$ corresponds to the actual phase at this temperature.

For the surface layer, which had the fastest cooling rate, $(U,Zr,Fe)O_2$ is a single phase, and there is little sign of phase segregation. The phases calculated via the Scheil equation (Case 1, Table 1) show that $(U,Zr,Fe)O_2$ is present as a single phase, but $(Zr,U)SiO_4$ formation is also predicted. Therefore, the phases calculated using the Scheil equation without $(Zr,U)SiO_4$ formation (Case 2, Table 1), as shown in Figure 3(b), are in good agreement with the analytical results.

Consequently, the simulation results under thermodynamic equilibrium conditions (Case 4, Table 1) correspond to the analytical phases for low cooling rates (below 10 K/s). For the quenching condition, the cooling rate was 85–100 K/s, and the simulation conditions with the Scheil equation (Case 1, Table 1) and without $(Zr,U)SiO_4$ formation (Case 2, Table 1) correspond to the analytical phases. These two types of conditions are therefore considered in the following plant-scale simulation.

3.2 Evaluation of solidification phases under 1F1 MCCI conditions

After the accumulation of molten corium on concrete in the PCV, ablated concrete is mixed into molten corium; the molten pool concentrates the concrete component due to the progression of the MCCI. In this case, the SiO_2 fractions in the concrete portions are constant in the product [25]. Therefore, the phase-changing behavior caused by the mixing of concrete and corium can be represented as a pseudobinary phase diagram of corium and concrete, as shown in Figure 5. Iron compounds are not shown in the diagram for simplicity and to aid understanding of the main phases. Figure 5 shows that the liquidus temperature decreases due to the increase in the concrete ratio, and solidification phases differ at the border, such that the molar ratio of corium and concrete in the mixture is approximately 1:1. Surplus ZrO_2, which forms $(Zr,U)SiO_4$, is consistently formed in the corium-rich region (shown in the left part of the diagram), while surplus SiO_2 is formed in the concrete-rich region (shown in the right part of the diagram). A similar tendency is reported in a ZrO_2–SiO_2 pseudobinary phase diagram [26]. This shows that the solidification phases are strongly affected by the mixing rate of ZrO_2–SiO_2.

More details of the solidification phases of molten core–concrete were estimated, as shown in Figure 6. Figure 6 shows the mass fraction of the solidification phases as a function of temperature. Figure 6(a) presents the calculation results for significant concrete ablation, with medium oxidation; the initial corium is UO_2–ZrO_2–Fe–Cr–Ni, under equilibrium conditions. U is included only in $(Zr,U)SiO_4$ or $(U,Zr)O_2$. These results correspond to the test

products of VE-U1 (all cases in Table 1). The molar fractions of UO_2 and ZrO_2 in fcc-$(U,Zr)O_2$ are shown in Figure 7 to aid understanding of the formation behaviors of these phases. The ratio of UO_2 to ZrO_2 during the initial solidification at 2,200–2,000 K is approximately 1:1, while the ratio of ZrO_2 decreases with the formation of $(Zr,U)SiO_4$ at 2,000–1,500 K. Subsequently, almost all the ZrO_2 separates from $(U,Zr)O_2$ at 1,500 K. Below 1,500 K, all the ZrO_2 separates from $(U,Zr)O_2$ and binds to SiO_2, thereby forming $(Zr,U)SiO_4$. This demonstrates that $(Zr,U)SiO_4$ is thermodynamically more stable than fcc-$(U,Zr)O_2$ for Zr.

Other common oxide phases that do not contain U and Zr are $CaAl_2Si_2O_8$ (anorthite), SiO_2 (quartz, tridymite), and $CaSiO_3$ (wollastonite). The formation of SiO_2 and absence of ZrO_2 demonstrate that this condition corresponds to the concrete-rich case (shown in Figure 5). The metallic phase is composed of the Fe–Ni alloy. The Cr in the initial Fe–Cr–Ni alloy is oxidized and forms Cr_2FeO_4, which has a spinel structure. The reaction and oxidation behavior of the Si-containing Fe–Cr–Ni alloy is discussed in section 3.4.

The volume of the ablated concrete considered in Figure 6(b) is 65% of that considered in Figure 6(a). Figure 6(b) shows that the mass fractions of $(U,Zr)O_2$ and $(Zr,U)SiO_4$ increase, while SiO_2 decreases in comparison with Figure(a). The other phases show a similar trend. The ablated concrete volume mainly affects the amount of solid phases and has a negligible effect on the species of the solid phase. This is also confirmed by the data presented in Figure 5. In Figure 6(c), which shows a less oxidized condition than that in Figure 6(a); the initial corium is UO_2–Zr–Fe–Cr–Ni, the mass fraction of Fe–Ni is lower, and the formation of the Fe–Si alloy and its compounds is confirmed. Under these conditions, oxidation affects the metallic phases, such as the Fe–Ni–Si phase. SiO_2 in the concrete is reduced to Si by Zr in corium and forms metallic phases with Fe–Cr–Ni, then Cr and Si are oxidized, as shown in Figure 2. Figure 6(d) shows an even more oxidized condition than that shown in Figure 6(a); the initial corium is UO_2–ZrO_2–Fe_2O_3−Cr_2O_3−NiO, which shows that all the metallic phases have been oxidized and that all Fe atoms are now incorporated in Cr_2FeO_4. Moreover, a portion of UO_2 is oxidized to U_4O_9, and $UCaO_4$ is also produced.

The phases evaluated using the Scheil equation are shown in Figure 6(e) and (f). A large portion of U and Zr form cubic $(U,Zr)O_2$ and the formation of $(Zr,U)SiO_4$ is drastically decreased, as shown in Figure 6(e). On the other hand, the formation of $(Zr,U)SiO_4$ is not taken into account in Figure 6(f). $(U,Zr)O_2$, which has a tetragonal structure, forms instead of $(Zr,U)SiO_4$ in this case. The other phases in these panels are similar to those shown in Figure 6(a).

The molar fractions of $USiO_4$ in $(Zr,U)SiO_4$ are shown in Figure 8. The decomposition temperature of $(Zr,U)SiO_4$ is in the range 1,875–1,975 K. The molar fraction of $USiO_4$ in

$(Zr,U)SiO_4$ is 19–27 mol.%. This ratio is larger than that of Chernobyl's LFCM and synthesized zircon, which is 5–10 mol.% [12, 27]. It is considered that the formation of $(Zr,U)SiO_4$ by thermodynamic dissolution of U from an U-Zr-Si-O melt requires more than a few days which was the condition for Chernobyl's LFCM formation. Details of the formation process of $(Zr,U)SiO_4$ are discussed in the next section.

3.3 Oxidation and reaction of U-containing phases

The data presented in Figure 6 confirm that UO_2 mainly reacts with ZrO_2 and SiO_2. Only under the most oxidative conditions, as shown in Figure 6(d), does UO_2 react with CaO to form $UCaO_4$. Therefore, the temperature and oxygen-potential dependence of the phase changes of UO_2−ZrO_2−SiO_2 are presented in Figure 9 to aid understanding of the behavior of U in the MCCI product under thermodynamic equilibrium conditions. The mixing ratios of UO_2, ZrO_2, and SiO_2 are the same as those given in Table 5 (a) and Figure 6(a). The general trends in the phase changes are as follows. As shown in the lower-right part of the figure, at a high temperature and low oxygen potential, all Si atoms are contained in the liquidus phase and U is present in the form of fcc-$(U,Zr)O_2$ and tet-$(U,Zr)O_2$. As shown in the middle range of the figure, U forms fcc-$(U,Zr)O_2$ and $(Zr,U)SiO_4$. Under these conditions, tet-$(U,Zr)O_2$ reacts with SiO_2 and forms $(Zr,U)SiO_4$. The crystal structure of $ZrSiO_4$ is tetragonal. In the low temperature and high oxygen-potential regime (upper-left part of the figure), U forms either $(Zr,U)SiO_4$ and U_4O_9 or U_3O_8.

From these results, the oxidation behavior of UO_2–ZrO_2–SiO_2 in this case can be described as follows:

> Liquid → Liquid, fcc-$(U,Zr)O_2$, and tet-$(U,Zr)O_2$ → fcc-$(U,Zr)O_2$ and $(Zr,U)SiO_4$ → $(Zr,U)SiO_4$ and U_4O_9 → $(Zr,U)SiO_4$ and U_3O_8

The decomposition temperature of $(Zr,U)SiO_4$ decreases with the oxygen potential at pressures below 10^{-14} atm. The decomposition temperature of $(Zr,U)SiO_4$ between 10^{-14} and 10^{-4} atm remains stable in the range 2,060–2,070 K. This temperature is slightly higher than the decomposition temperature of $(Zr,U)SiO_4$ (shown in Figure 8). It has been predicted that other components, such as Al_2O_3, decrease the decomposition temperature of $(Zr,U)SiO_4$ [12].

3.4 Oxidation and reaction of metallic phases

The metallic phase is composed of Fe, Cr, Ni, and Si. Si is generated via a redox reaction of SiO_2 with Zr. The oxidation behaviors of the Fe–Cr–Ni alloy and Fe–Si are shown in Figures 10 and 11, respectively.

In Figure 10, the solidus temperature remains constant at ~1,800 K, while the oxygen

potential is varied. Conversely, the liquidus temperature strongly depends on the oxygen potential. Only for low oxygen potentials are Fe, Cr, and Ni atoms contained in the metallic phase. The liquidus temperature remains stable at 1,740–1,750 K. The general oxidation tendencies of the Fe–Cr–Ni alloy can be expressed as follows:

Fe−Cr−Ni alloy → Fe−Ni alloy and Cr_2O_3 → Fe–Ni alloy and spinel structured materials such as Cr_2FeO_4 → spinel structured materials such as Cr_2FeO_4 and Fe_2NiO_4 → spinel- and rhombohedral-structured materials such as $(Fe,Ni)_3O_4$ and $(Fe,Cr)_2O_3$. In the case where molten Fe–Cr–Ni is oxidized above 1,740–1,750 K, spinel structured materials form without formation of Cr_2O_3. This result is good agreement with thermodynamic calculation results under VULCANO VBS-U3 conditions [28]. Moreover, this indicates the possibility that Cr_2O_3 layers surrounding steel at the melt-steel interface in VBS-U3 samples were produced by oxidation of solid Fe–Cr–Ni below 1,740–1,750 K; on the other hand, $(Fe,Cr)_3O_4$ and Fe_2O_3 were produced at the gas bubble-metal interface by oxidation of liquid Fe–Cr–Ni above 1,740–1,750 K.

The oxidation behavior of Fe–Si is shown in Figure 11. The solidus and liquidus temperatures are highly dependent on the oxygen potential. The oxidation behavior of Fe–Si can be expressed as follows:

Fe–Si → Liquid and SiO_2 → Fe and SiO_2 → $FeSiO_4$ and SiO_2 → Fe_3O_4 and SiO_2 → Fe_2O_3 and SiO_2.

The collection of thermodynamic data on Cr−Ni−Si−O should continue, because the calculations on the oxidation behavior of Fe−Cr−Ni−Si show poor results.

4. Discussion of the MCCI progression under 1F1 conditions

Physicochemical phenomena during the MCCI have been modeled on the basis of various experimental data sets and have helped to refine the simulation codes [10]. The results of this modeling are useful in aiding understanding of heat transfer from the molten core–concrete to the outer environment, concrete, or upper cooling water; furthermore, these results show that the temperature difference between these materials generates a crust, which acts as an insulating layer at these interfaces [29]. Concrete compositions in the molten core–concrete are concentrated via concrete ablation, and the liquidus temperature of the molten core–concrete decreases, with an increase in the concrete fraction, as shown in Figure 5. Solidification of the molten core–concrete increases with decreasing liquidus temperature and the crust thickness increases.

In the case of the estimated 1F1 conditions, when the temperature of the crust decreases to the concrete liquidus temperature, which is about 1,700 K under the estimated 1F1 conditions, the rate of concrete ablation would decrease. Moreover, when it decreases to

the concrete solidus temperature, which is about 1,400 K under the estimated 1F1 conditions, concrete ablation ceases. When this occurs, the temperature of the molten core–concrete decreases slowly and it solidifies owing to decay heat and the adiabatic effect of the crust.

The phases calculated via the Scheil equation, shown in Figure 6(e) and (f), adequately explain crust formation at the molten pool-atmosphere interface; i.e., the crust is formed under quenching conditions because of the temperature difference between the molten pool and either air or water. The initial solidification phase of the crust is fcc-$(U,Zr)O_2$, and there is only a small amount of phase segregation in U-rich cubic and Zr-rich tetragonal $(U,Zr)O_2$. Since the amount of $(Zr,U)SiO_4$ is overestimated using the Scheil equation, as detailed in Table 1, formation of $(Zr,U)SiO_4$ will be limited. Therefore, most U and Zr atoms are incorporated in fcc-$(U,Zr)O_2$. After solidification of $(U,Zr)O_2$, $CaAl_2Si_2O_8$ and SiO_2 are generated, in that order. In this case, the kinetics of $CaAl_2Si_2O_8$ crystal growth and dissolution of U in SiO_2 should be discussed on the basis of experimental data or by using other methods.

Solidification of the entire molten pool requires a considerable amount of time (i.e., days) and tends toward the thermodynamic equilibrium condition. Therefore, the solidification phases of the bulk of the molten pool were estimated under equilibrium conditions. When the oxide and metallic phases are mixed and form a molten pool, this molten pool stratifies into two layers, one of which is an oxide-rich liquid and the other an oxide-poor liquid, because these liquid phases have a miscibility gap, as shown in Figure 6. In the later phases of the MCCI, the oxide-rich liquid phase becomes lighter than the oxide-poor phase; thus, the oxide-rich liquid rises and becomes the upper layer, whereas the oxide-poor liquid sinks and becomes the lower layer [30]. The main solid phases in a molten pool above 1,745 K are fcc-$(U,Zr)O_2$, $(Zr,U)SiO_4$, and two liquid phases. The fraction of $(Zr,U)SiO_4$ in the solid phases increases below 1,745 K because the ZrO_2 phase separates from fcc-$(U,Zr)O_2$, along with a small amount of U, which subsequently forms $(Zr,U)SiO_4$ with SiO_2. In this temperature range, the oxide-poor liquid solidifies and a metallic phase containing mainly Fe and Ni is formed. Then, light oxide phases, such as $CaAl_2Si_2O_8$, SiO_2, and $CaSiO_3$, solidify at approximately 1,700–1,400 K. The metallic phase of Fe–Si solidifies along with the light oxide phases at 1,400–1,500 K. The composition of this metallic phase is strongly dependent on the oxygen potential, as shown in Figures 10 and 11. When the oxygen potential is above 10^{-7} atm, all the metallic phases are oxidized. Under experimental conditions, however, the metallic layer remains after the MCCI phenomena [31]. Therefore, the experimental oxygen potential would be lower than 10^{-7} atm. On the other hand, the oxygen potential during a plant-scale MCCI is unknown and the oxidation situation of the

Fe–Cr–Ni alloy in the MCCI product in 1F1 can be used to elucidate the oxygen potential during a plant-scale MCCI.

The molten pool-concrete interface would be kept at a temperature in the vicinity of the concrete liquidus and solidus temperatures. In this region of the MCCI test products, a few millimeters of a corium-rich zone and a concrete-rich zone were confirmed to be formed by convection in the molten pool [25,32]. In the case of VB-U4 products, the average composition of $(U,Zr)O_2$ in the concrete-rich zone is around 40 wt%, and that in the corium-rich zone is 60–66 wt% [32]. If similar phenomena occurred in the 1F MCCI, then both zones would be included in the concrete-rich region in Figure 5. At the border between the corium-rich and concrete-rich regions, the concrete represents about 25 wt% of the total composition. Therefore, larger amounts of fcc-$(U,Zr)O_2$ and $(Zr,U)SiO_4$ will be contained in the corium-rich zone compared to the concrete-rich zone, and larger amounts of Al_2O_3, anorthite, and SiO_2 will be found in the concrete-rich zone.

The phase-change behaviors during solidification of the MCCI products under 1F1 conditions are discussed above. The performance of the fuel removal tools depends on their mechanical and thermophysical properties as well as on the phases of the MCCI products. These results and the physical properties database will be useful for the development of removal tools.

5. Conclusion

In this study, the solidification phases of molten core–concrete were estimated via a thermodynamic equilibrium calculation. It was found that most U and Zr atoms are involved in the formation of $(U,Zr)O_2$ or $(Zr,U)SiO_4$. The fractions of $(U,Zr)O_2$ and $(Zr,U)SiO_4$ in the material depend on the cooling rate. The crystal structure of a portion of the fcc-$(U,Zr)O_2$ changes to tet-$(U,Zr)O_2$, which contains a high fraction of Zr and forms $(Zr,U)SiO_4$ with SiO_2. Because this process requires a relatively long time, the formation of $(Zr,U)SiO_4$ is limited under quenching conditions, such as when top surface crust formation occurs during estimated 1F MCCIs. Moreover, most Zr becomes incorporated in $(Zr,U)SiO_4$, rather than in fcc-$(U,Zr)O_2$ in the bulk of the molten pool when the cooling rate is slow. Other common oxide phases are $CaAl_2Si_2O_8$, SiO_2, and $CaSiO_3$. The main components of the metallic phases under estimated 1F MCCI conditions are Fe, Cr, Ni, and Si. Although these form various metallic and oxide phases depending on the oxygen potential, further thermodynamic data should be obtained experimentally to evaluate their exact equilibrium phases. Consequently, the oxidation conditions of Fe–Cr–Ni–Si can be compared to the analytical results for the 1F MCCI products, thereby clarifying the local oxygen potential. These findings would facilitate a precise understanding of the 1F MCCI progression.

References

[1] B. Spindler, B. Tourniaire, J.M. Seiler, Simulation of MCCI with the TOLBIAC-ICB code based on the phase segregation model, Nuclear Engineering and Design 236 (2006) 2264-2270.

[2] H.J.Allelein, K.Neu, J.P.Van Dorsselaere, K. Müller, P. Kostka, M. Barnak, et al., European validation of the integral code ASTEC (EVITA), Nuclear Engineering and Design 221 (2003) 95–118.

[3] Y.Maruyama, Y. Kojima, M. Tahara, H. Nagasaka, M. Kato, A.A. Kolodeshnikov, et al., A study on concrete degradation during molten core/concrete interactions, Nuclear Engineering and Design 236 (2006) 2237–2244.

[4] K.Yano, T.Kitagaki, H.Ikeuchi, R.Wakui, H.Higuchi, N.Kaji, et al., Direction on Characterization of Fuel Debris for Defueling Process in Fukushima Daiichi Nuclear Power Station, Proceedings of Global 2013, Salt Lake City, Utah, September 29-October 3, (2013) 1554-1559.

[5] H. Ikeuchi, M. Ishihara, K. Yano, N. Kaji, Y. Nakajima, T. Washiya, Dissolution behavior of (U,Zr)O_2-based simulated fuel debris in nitric acid, Journal of Nuclear Science and Technology 51 (7–8) (2014) 996-1005.

[6] Akers DW, Carlson ER, Cook BA, Ploger SA, Carlson JO, TMI-2 core debris grab samples examination and analysis: Part 1, EG&G Idaho. Inc., United States, 1986, Report GEND-INF-075-Pt.1.

[7] Akers DW, Carlson ER, Cook BA, Ploger SA, Carlson JO. TMI-2 core debris grab samples examination and analysis: Part 2, EG&G Idaho. Inc., United States, 1986, Report GEND-INF-075-Pt.2.

[8] P.D.W. Bottomley, B. Clément, T. Haste, D. Jacquemain, D.A. Powers, M. Schwarz, et al., (eds.), Phébus FP Final Seminar Special Issue, Annals of Nuclear Energy 61 (2013) 1-230.

[9] Main Results of the First Phase of MASCA Project, RRC Kurchatov Institute, OECD MASCA Project integrated report, (2004).

[10] B.R. Sehgal edit., Nuclear safety in light water reactors, Elsevier, Waltham, U.S., 2012 (Chapter 4).

[11] J.J. Foit, M. Fischer, C. Journeau, G. Langrock, Experiments on MCCI with oxide and steel, Annals of Nuclear Energy 74 (2014) 100-109.

[12] É.M.Pazukhin, Fuel containing lavas of the Chernobyl NPP fourth block, Radiochemistry 36 (2) (1994) 109-154.

[13] C.Journeau, F.Sudreau, S.Magne, G.Cognet, Physico-chemical analyses and solidification path reconstruction of multi-component oxidic spread melts, Materials

Science and Engineering, A299 (2001) 249-266.
[14] R.G.J. Ball, M.A. Mignanelli, T.I. Barry, J.A. Gisby, The calculation of phase equilibria of oxide core-concrete systems, Journal of Nuclear Materials, 201 (1993) 238-249.
[15] C.W. Bale, E. Bélisle, P. Chartrand, S.A. Decterov, G. Eriksson, A.E. Gheribi, et al., FactSage thermochemical software and databases, 2010-2016, CALPHAD 54 (2016) 35-53.
[16] B. Cheynet. NUCLEA. 73 pages. 2007. <hal-00165418>
[17] E.scheil, Bemerkungen zur schichtkristallbildung, Zeitschrift für Metallkunde. 34 (1942) 70-72.
[18] Latest analyses result with MAAP 5 [Internet]. Tokyo: Tokyo Electric Power Company [cited 2016 Jul 11]. Available from: http://www.tepco.co.jp/cc/press/betu14_j/images/140806j0106.pdf
[19] The Evaluation Status of Reactor Core Damage at Fukushima Daiichi Nuclear Power Station Units 1 to 3 [Internet]. Tokyo: Tokyo Electric Power Company [cited 2016 Jul. 11]. Available from: http://www.tepco.co.jp/nu/fukushima-np/images/handouts_111130_09-j.pdf.
[20] The interactive Ellingham diagram [Internet]. Cambridge: University of Cambridge [cited 2016 Aung. 18]. Available from: http://www.doitpoms.ac.uk/tlplib/ellingham_diagrams/interactive.php.
[21] T.B.Lindemer, T.M.Besmann, Chemical thermodynamic representation of $<UO_{2\pm x}>$, Journal of Nuclear Materials 130 (1985) 473488.
[22] M.Ozawa, K.Yabuki, A.Shimada, T.Ueno, Chemical component analysis of core coring samples at reactor building in Fukushima-1 Nuclear Power Plant, 2014 Annual meeting of AESJ, Tokyo, March 26-28, (2014) G35.
[23] K.Y.Shin, S.B. Kim, J.H. Kim, M. Chung, P.S. Jung, Thermo-physical properties and transient heat transfer of concrete at elevated temperature, Nuclear Engineering and Design 212 (2002) 233–241.
[24] B.E. Burakov, M.I. Ojovan, W.E. Lee, Crystallin Materials for actinide immobilization, Imperial College Press, London, U.K., 2011 (Chapter 3).
[25] C. Journeau, P. Piluso, J.F. Haquet, E. Boccaccio, V. Saldo, J.M. Bonnet, et al., Two-dimensional interaction of oxidic corium with concretes: The VULCANO VB test series, Annals of Nuclear Energy 36 (2009) 1597-1613.
[26] A.M. Evans, J.P.H. Williamson, F.P.Glasser, Microstructure of plasma dissociated zircon and liquid immiscibility in the ZrO_2-SiO_2 system, Journal of Material Science 15 (1980) 2325-2330.
[27] S.V. Ushakov, W. Gong, M.M. Yagovkina, K.B. Helean, W. Lutze and R.C. Ewing, Solid

solutions of Ce, U and Th in zircon, Ceramic transactions 93 (1999) 357-363.

[28] M.S. Brusset, P. Piluso, M.B. Pichelin, P.D. Bottomley and T. Wiss, Steel oxidation phenomena during Molten corium siliceous concrete interaction (MCCI), Journal of alloys and compounds 622 (2015) 1005-1012.

[29] J.M. Seiler, Phase segregation model and molten pool thermal-hydraulics during molten core-concrete interaction, Nuclear Engineering and Design 166 (1996) 259-267.

[30] B. Tourniaire, J.M. Bonnet, Study of the mixing of immiscible liquids by sparging gas results of the BALISE experiments. Proceedings of the 10th International Topical Meeting on Nuclear Reactor Thermal Hydraulics (NURETH 10), Seoul, Korea, October 5–9, (2003).

[31] C.Journeau, P.Piluso, J.F.Haquet, S.Saretta, E.Boccaccio, J.M. Bonnet, Oxide-metal corium-concrete interaction test in the VULCANO facility, Proceedings of ICAPP 2007, Nice, France, May 13-18, (2007) 7328.

[32] C. Journeau and P.Piluso, Core concrete interaction, Elsevier Ltd., Amsterdam, Netherlands, 2012 (Comprehensive nuclear materials, Chapter 2.25).

Table 1 Comparison of the analytical and calculated phases of the VE-U1 test samples

Position and cooling rate	Test samples [11]	(Calculation condition) Calculated phases and Mass fraction at 1,000 [K]
Surface 85–100 K/s	$(U_{0.33},Zr_{0.47},Fe_{0.20})O_{1.83}$ $(U_{0.42},Zr_{0.55},Fe_{0.03})O_{1.83}$ SiO_2	Case 1: Scheil equation 42.7 wt% cubic-$(U_{0.59},Zr_{0.34},Fe_{0.05})O_2$ 34.2 wt% $(Zr_{0.74},U_{0.26})SiO_4$ 8.0 wt% Fe_3O_4 10.4 wt% cristobalite-SiO_2 Case 2: Scheil equation without $(Zr,U)SiO_4$ (see Figure 3 (b)) 64.3 wt% cubic-$(U_{0.47},Zr_{0.47},Fe_{0.05})O_2$ 6.7 wt% Fe_3O_4 18.4 wt% cristobalite-SiO_2
Middle ~10 K/s	$(U_{0.78},Zr_{0.12},Fe_{0.10})O_{1.87}$ $(U_{0.26},Zr_{0.65},Fe_{0.09})O_{1.60}$ SiO_2 $Fe_{1.2}SiO_{3.56}$	Case 3: Equilibrium without $(Zr,U)SiO_4$ 44.5 wt% cubic-$(U_{0.94},Fe_{0.03,}\ Mg_{0.02})O_2$ 22.8 wt% ZrO_2 19.1 wt% quartz-SiO_2 8.4 wt% Fe_3O_4 4.6 wt% Fe_2SiO_4
Bottom Below 10 K/s	UO_2 $(U_{0.32},Zr_{0.82})SiO_{3.64}$ $(U_{0.13},Zr_{0.98})SiO_{3.75}$ SiO_2 $Fe_{2.2}SiO_{3.76}$	Case 4: Equilibrium (see Figure 3(a)) 28.9 wt% cubic-$(U_{0.94},Fe_{0.03,}\ Mg_{0.03})O_2$ 52.7 wt% $(Zr_{0.77},U_{0.23})SiO_4$ 4.5 wt% quartz-SiO_2 8.4 wt% Fe_3O_4 4.9 wt% Fe_2SiO_4

Table 2 Composition of the in-core material and corium

Components in RPV	Corium weight in an RPV [t]	Corium weight in a sump [t]	Components of simulation	Corium weight of simulation [t]
UO_2	79	9.3	UO_2	9.3
Zircalloy	32	3.8	Zr	3.8
Core Internals	18	2.1	SUS	2.1
Total	129	15.2	Total	15.2

Table 3 Estimated composition of 1F1 pedestal concrete [mass%]

	Al	Al_2O_3	Ca	CaO	Fe	Fe_2O_3	Si	SiO_2	Total
Analysis [20]	7.0	-	7.8	-	3.6	-	25	-	43.4
Estimated	-	13.2	-	10.9	-	5.1	-	53.5	82.7

Table 4 Ablation weights in a sump pit [t]

	SiO_2	CaO	Al_2O_3	Fe_2O_3
Square	9.6	2.0	2.4	0.9
Circle	6.2	1.3	1.5	0.6

Table 5 Calculation conditions and compositions for the solidification phases of 1F1 MCCI in Figure 6

Case	Mass fractions [%]									Solidification condition
	UO_2	Zr	ZrO_2	SUS	Oxidized SUS	SiO_2	CaO	Al_2O_3	Fe_2O_3	
a	29.6	-	16.2	6.7	-	30.6	6.4	7.6	2.9	Equilibrium
b	35.6	-	19.5	8.0	-	23.8	5.0	5.7	2.3	Equilibrium
c	30.9	12.6	-	7.0	-	31.9	6.6	8.0	3.0	Equilibrium
d	28.8	-	15.8	-	0.093	29.7	6.2	7.4	2.8	Equilibrium
e	29.6	-	16.2	6.7	-	30.6	6.4	7.6	2.9	Scheil equation
f	29.6	-	16.2	6.7	-	30.6	6.4	7.6	2.9	Scheil equation without $(Zr,U)SiO_4$

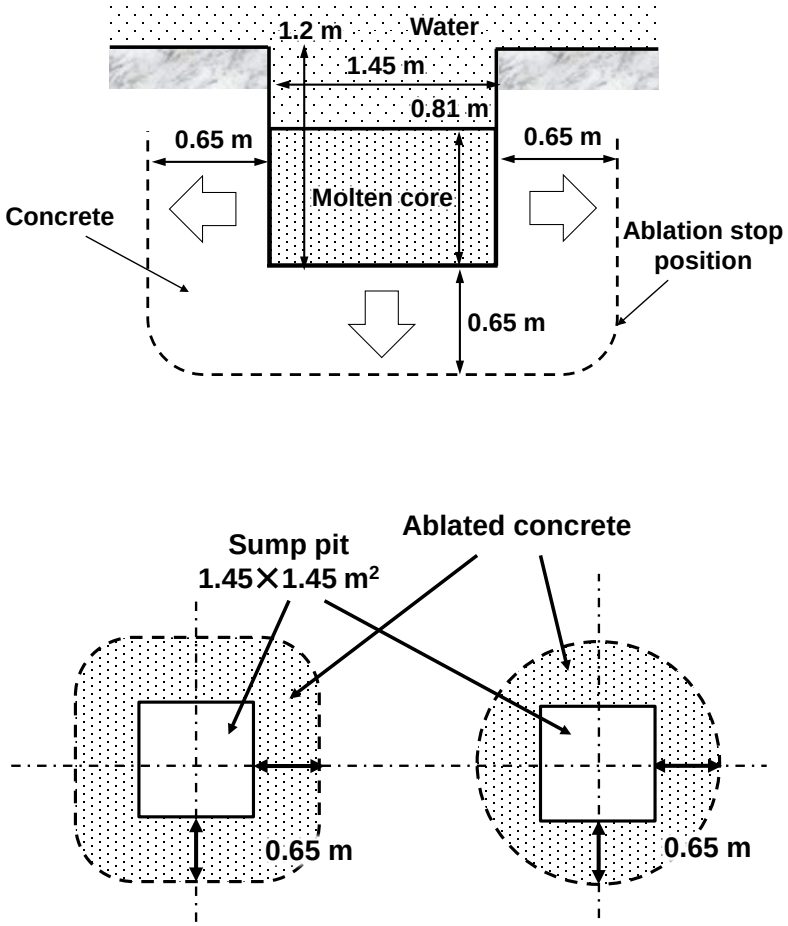

Figure 1 Ablated concrete around a sump pit in 1F1 pedestal

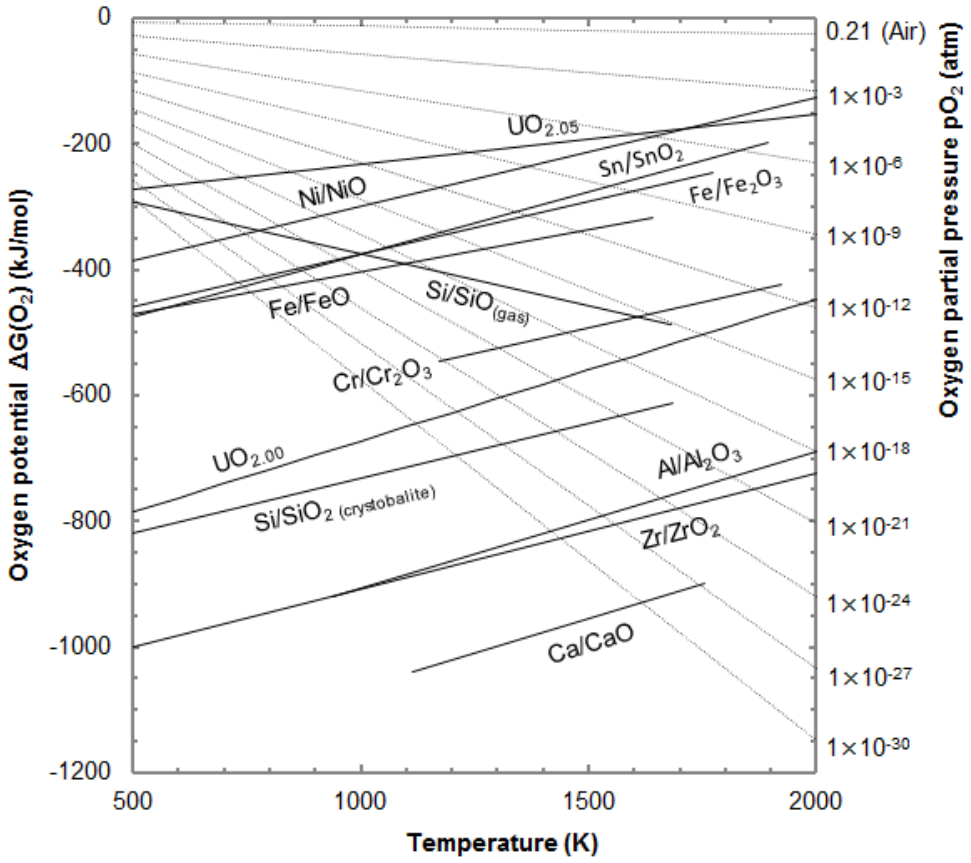

Figure 2 Ellingham diagram for molten core–concrete materials

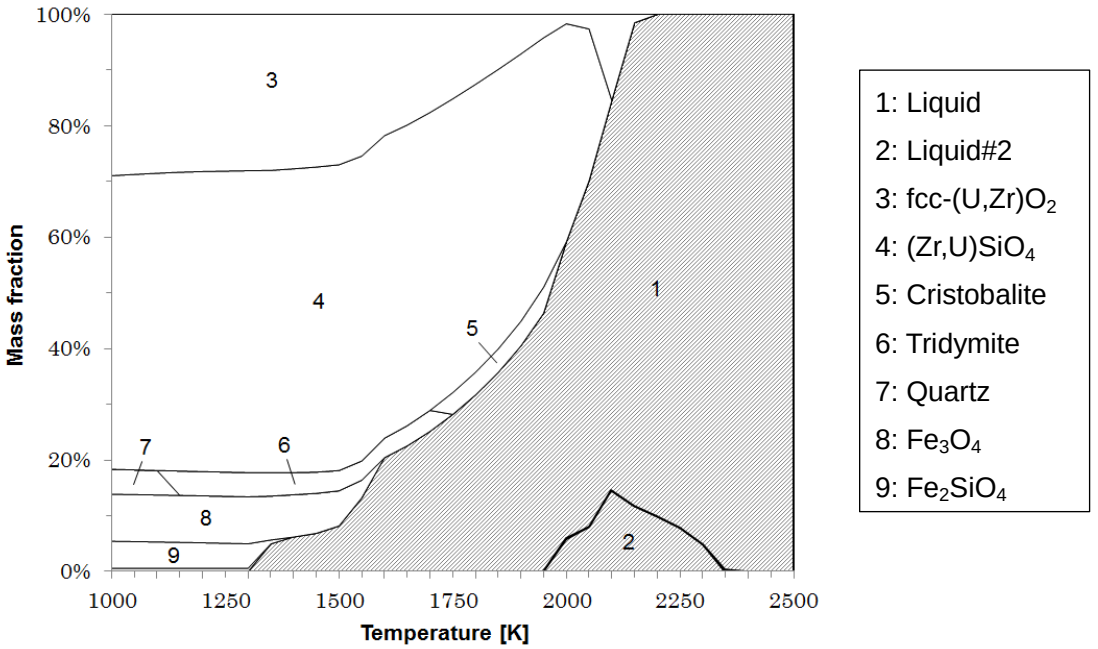

(a) Mass fraction of solidification phases under thermodynamic equilibrium conditions

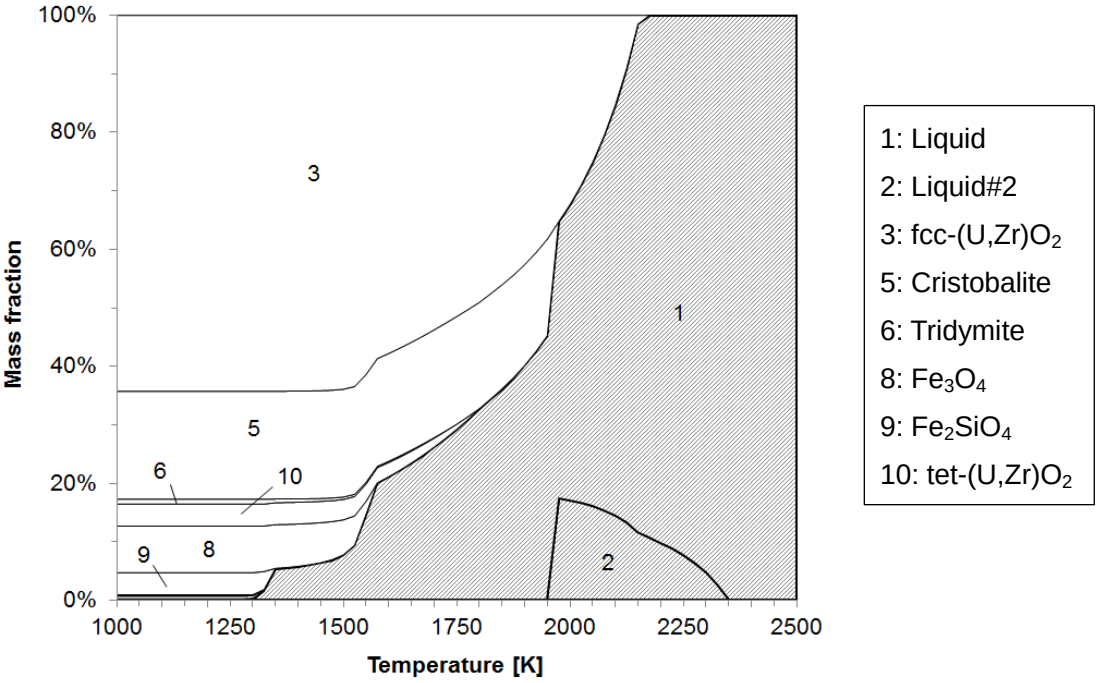

(b) Mass fraction of solidification phases using the Scheil equation without $(Zr,U)SiO_4$ formation

Figure 3 Mass fractions of the solidification phases of the VE-U1 experimental data (Shaded area: liquidus phase, other: oxide phase)

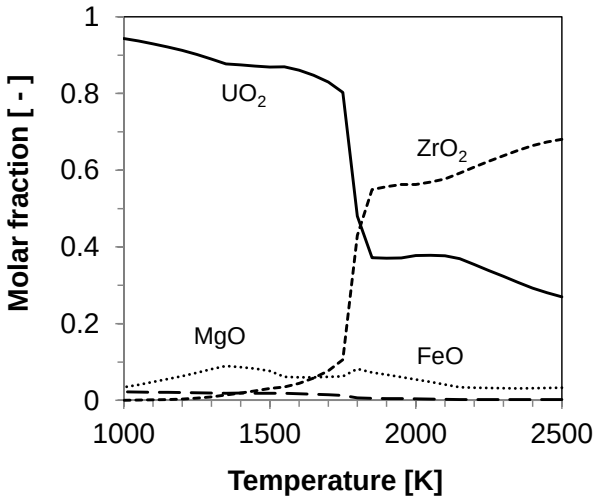

Figure 4 Molar fractions of $(U,Zr)O_2$ under the VE-U1 test conditions, corresponding to Case 3 in Table 1

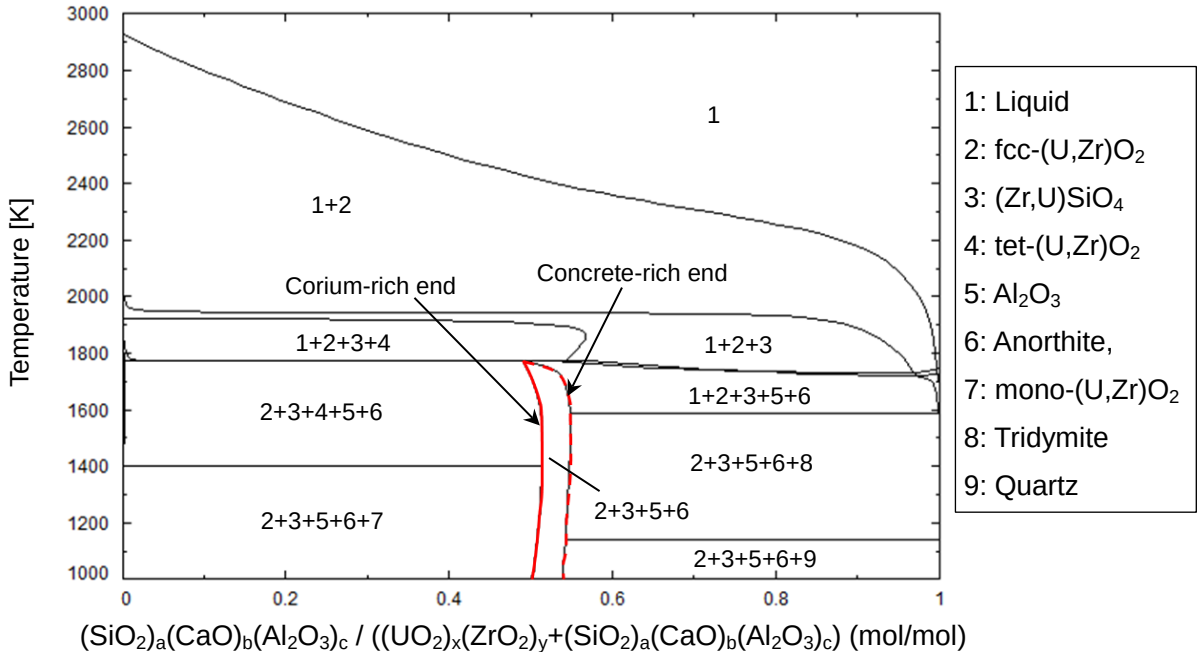

Figure 5 Pseudobinary phase diagram for corium–concrete
a: 0.686, b: 0.143, c: 0.171, x: 0.646, and y: 0.354

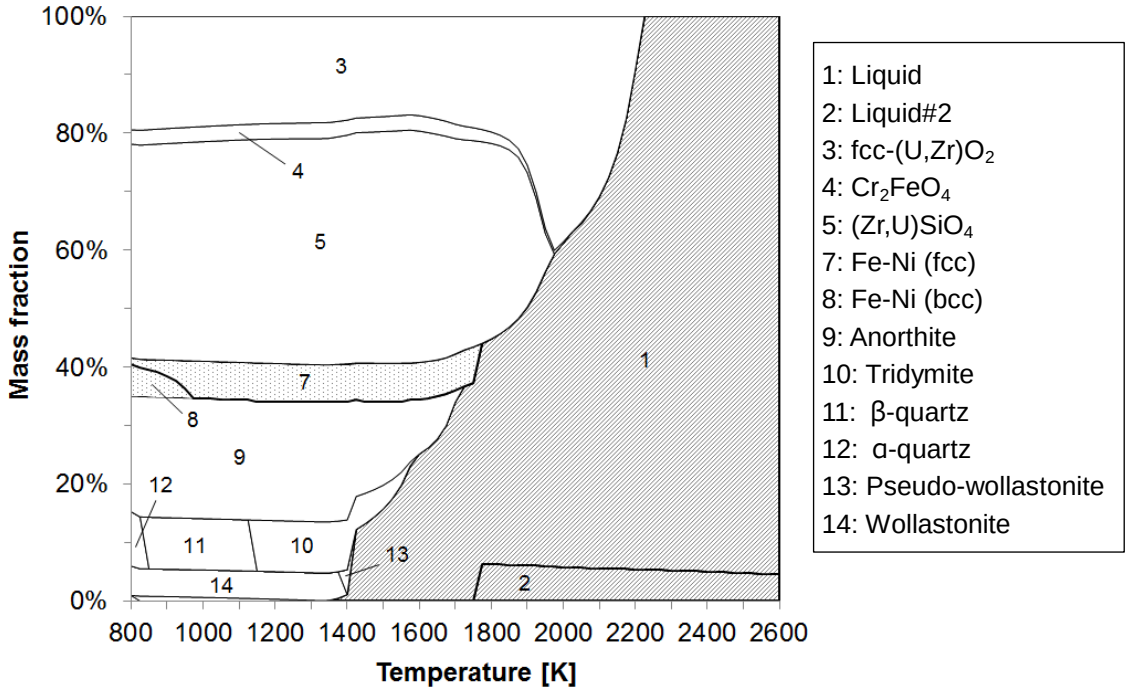

(a) UO_2–ZrO_2–Fe–Cr–Ni-concrete, square-shaped concrete ablation (left side in Figure 1) under equilibrium conditions

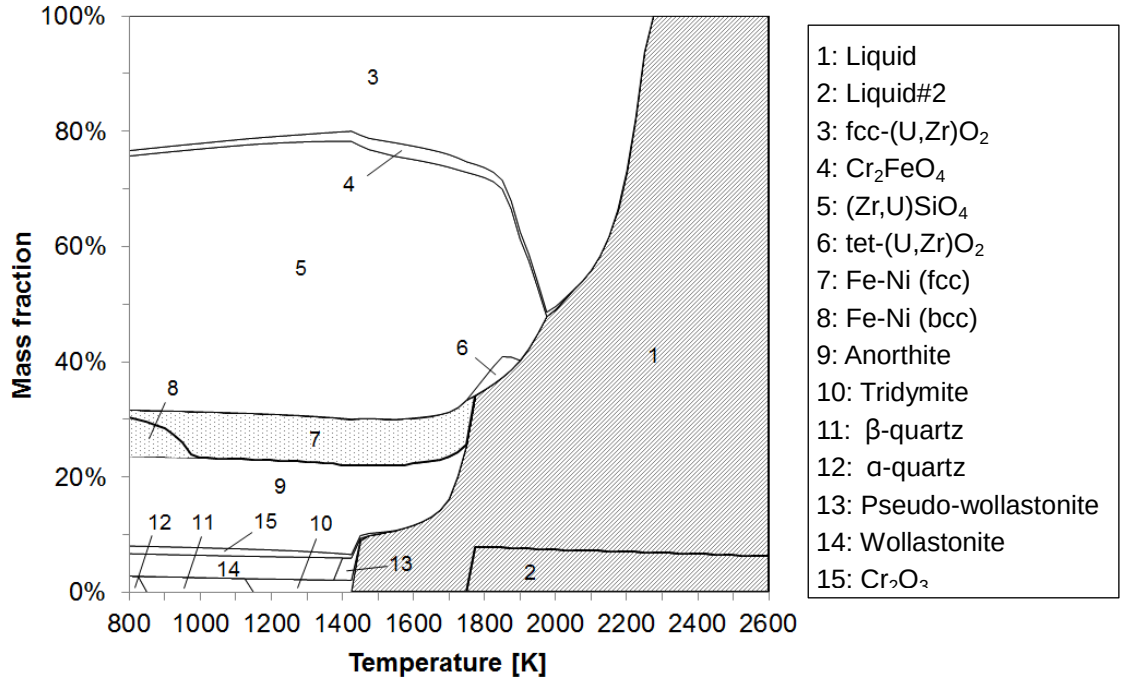

(b) UO_2–ZrO_2–Fe–Cr–Ni-concrete, circle-shaped concrete ablation (right side in Figure 1) under equilibrium conditions

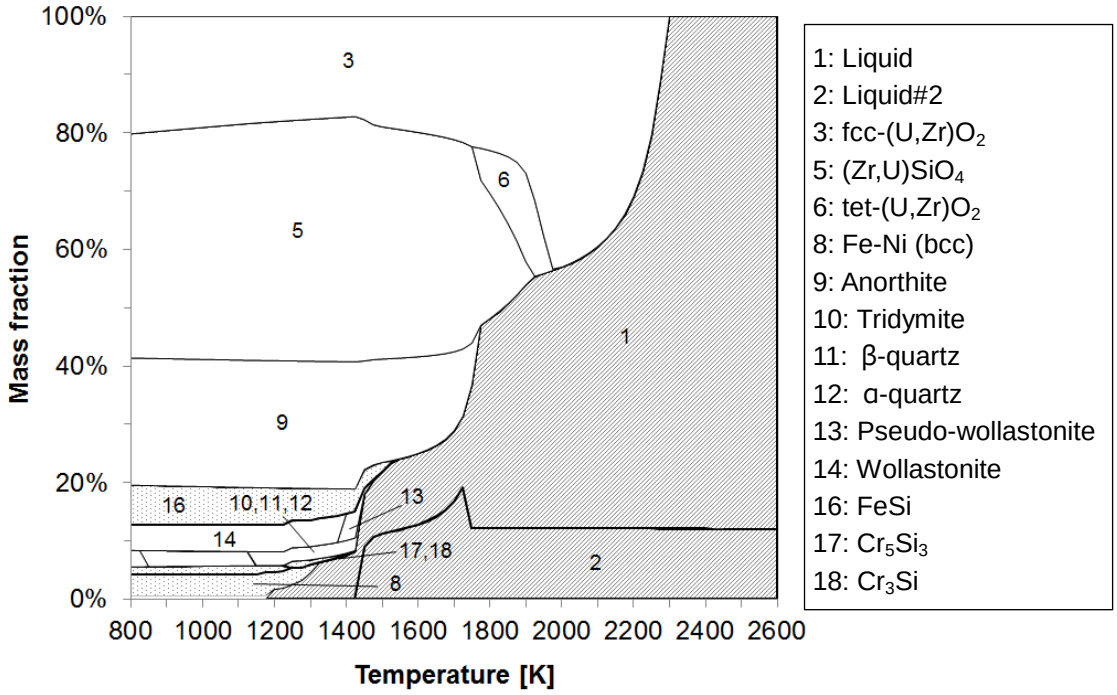

(c) UO_2–Zr–Fe–Cr–Ni-concrete, square-shaped concrete ablation (left side in Figure 1) under equilibrium conditions

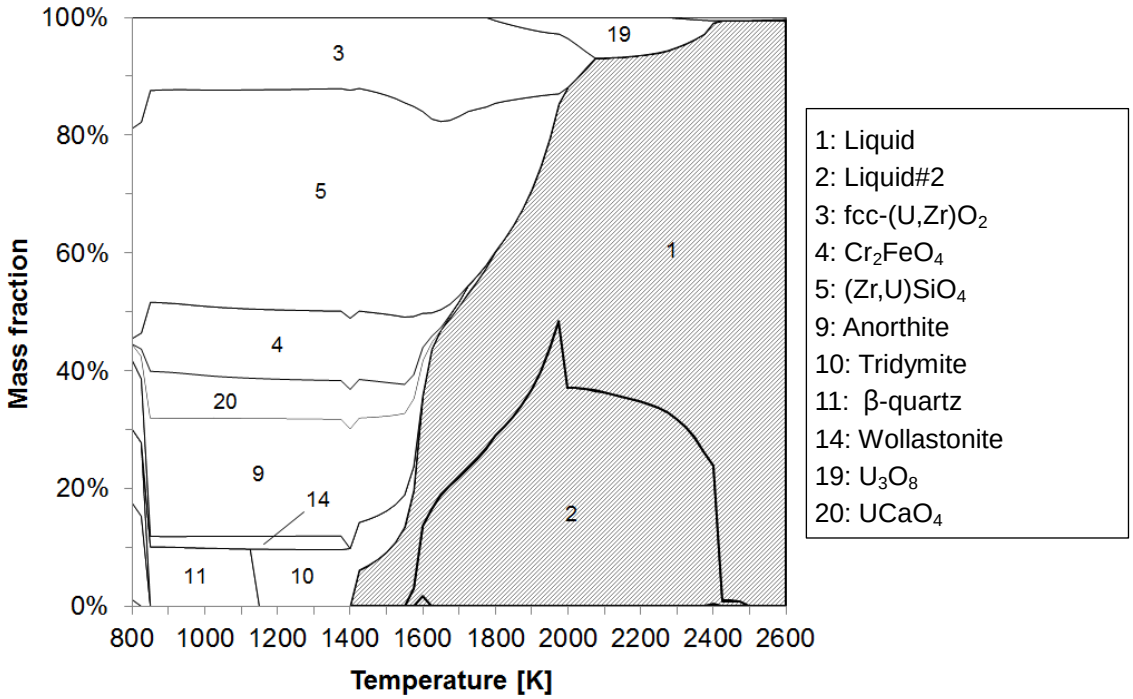

(d) UO_2-ZrO_2-Fe_2O_3-Cr_2O_3-NiO-concrete, square-shaped concrete ablation (left side in Figure 1) under equilibrium conditions

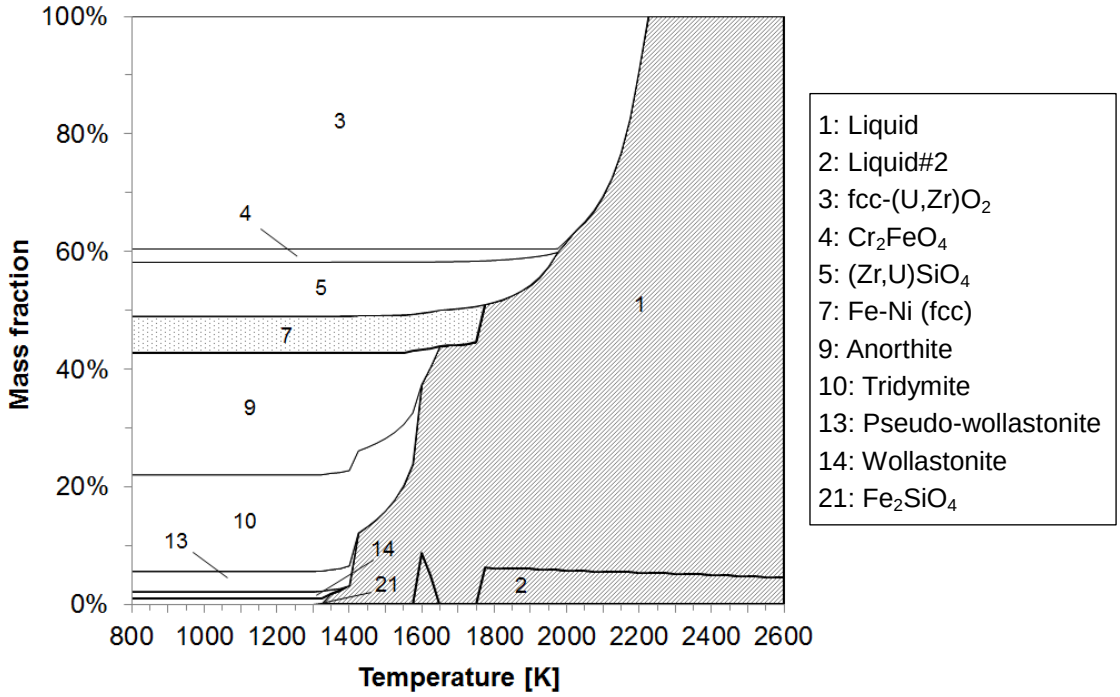

(e) UO_2–ZrO_2–Fe–Cr–Ni-Concrete, square-shaped concrete ablation (left side in Figure 1) using the Scheil equation

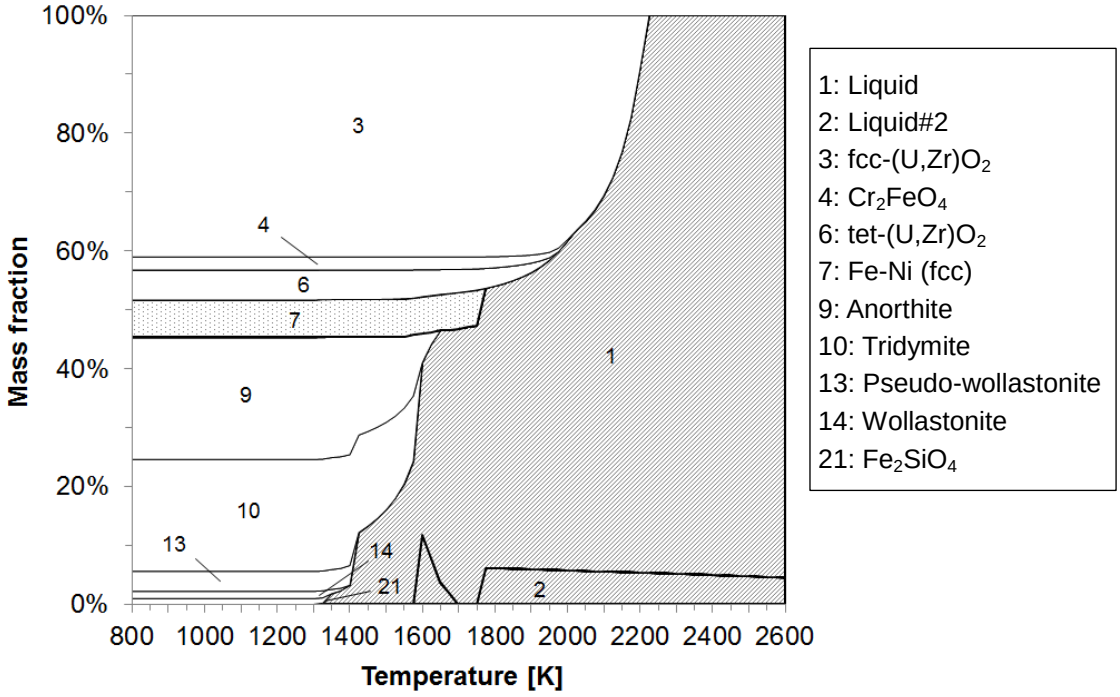

(f) UO_2–ZrO_2–Fe–Cr–Ni-Concrete, square-shaped concrete ablation (left side in Figure 1) using the Scheil equation without $(Zr,U)SiO_4$ formation

Figure 6 Mass fractions of the solidification phases of the 1F compositions listed in Table 5 (Shaded area: liquidus phase, dotted area: metallic phase, other: oxide phase)

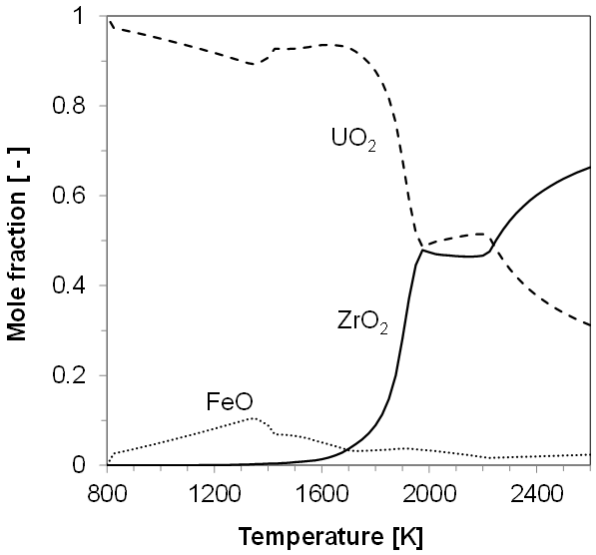

Figure 7 Molar fraction of UO_2, ZrO_2, and FeO in $(U,Zr)O_2$ at equilibrium for composition (a) in Table 5

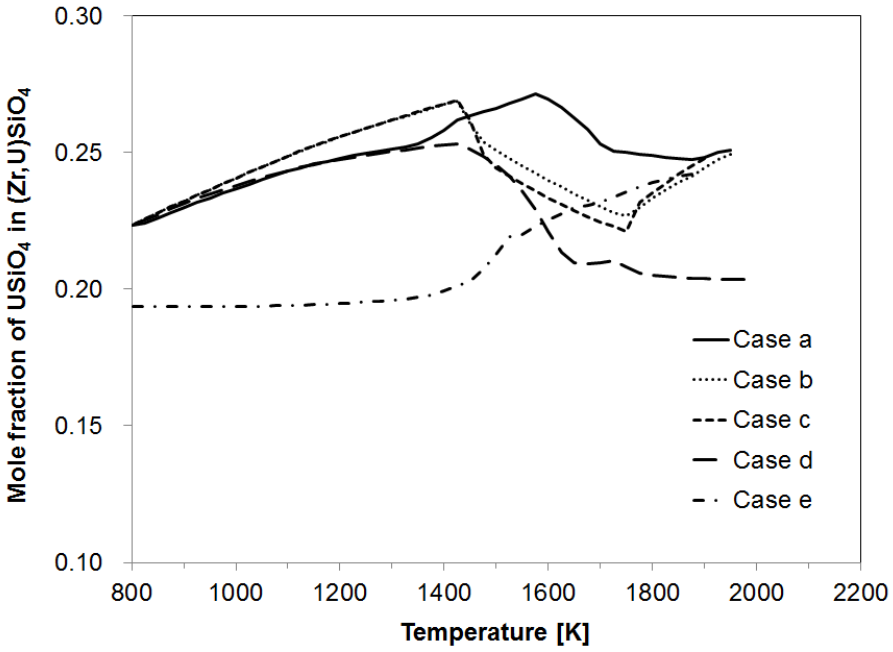

Figure 8 Temperature dependence of the molar fraction of $USiO_4$ in $(Zr,U)SiO_4$

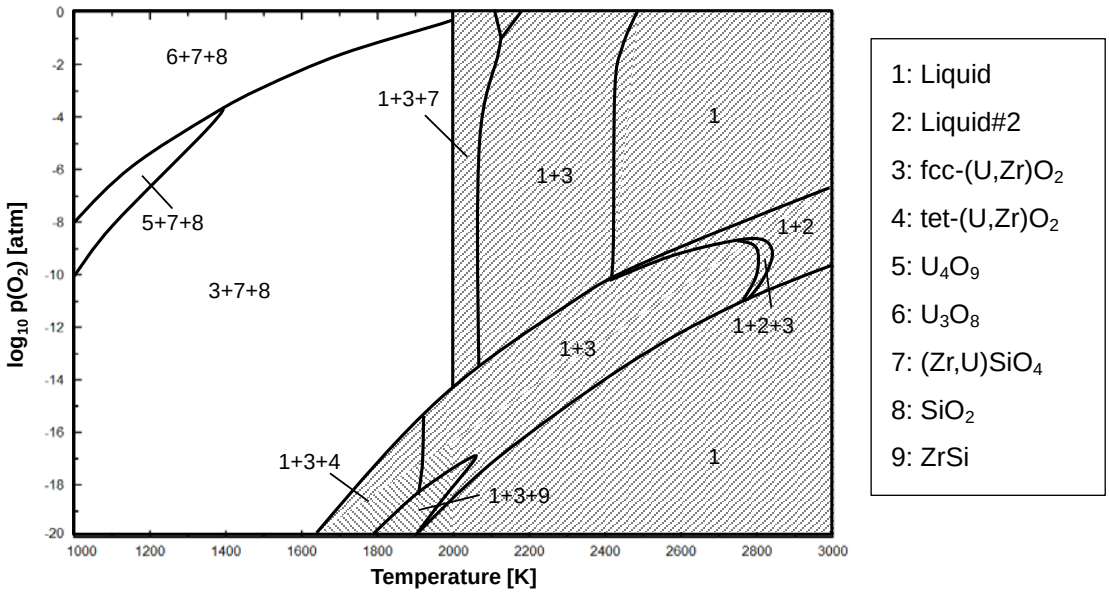

Figure 9 Oxygen-potential diagram of $(UO_2)_a(ZrO_2)_b(SiO_2)_c$

a: 0.38775, b: 0.2125, and c: 0.400

(Shaded area: liquidus phase or solid-liquid coexistence phase, other: oxide phase)

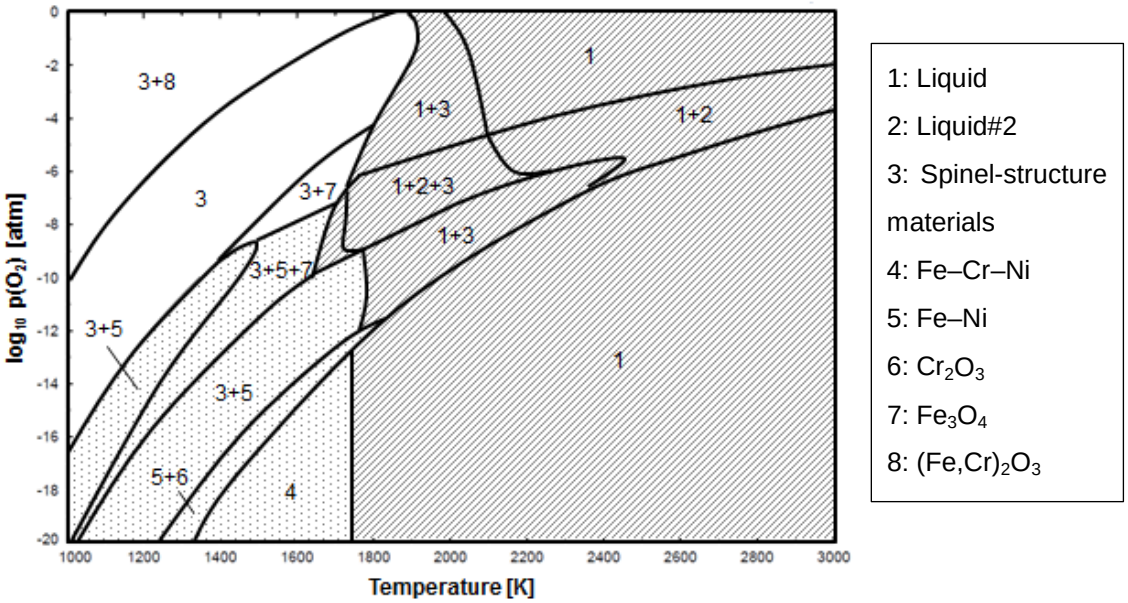

Figure 10 Dependence of the phase-change of the Fe_a–Cr_b–Ni_c alloy on oxygen potential and temperature

a: 0.74, b: 0.18, and c: 0.08

(Shaded area: liquidus phase or solid-liquid coexistence phase, dotted area: metallic phase or metal-oxide coexistence phase, other: oxide phase)

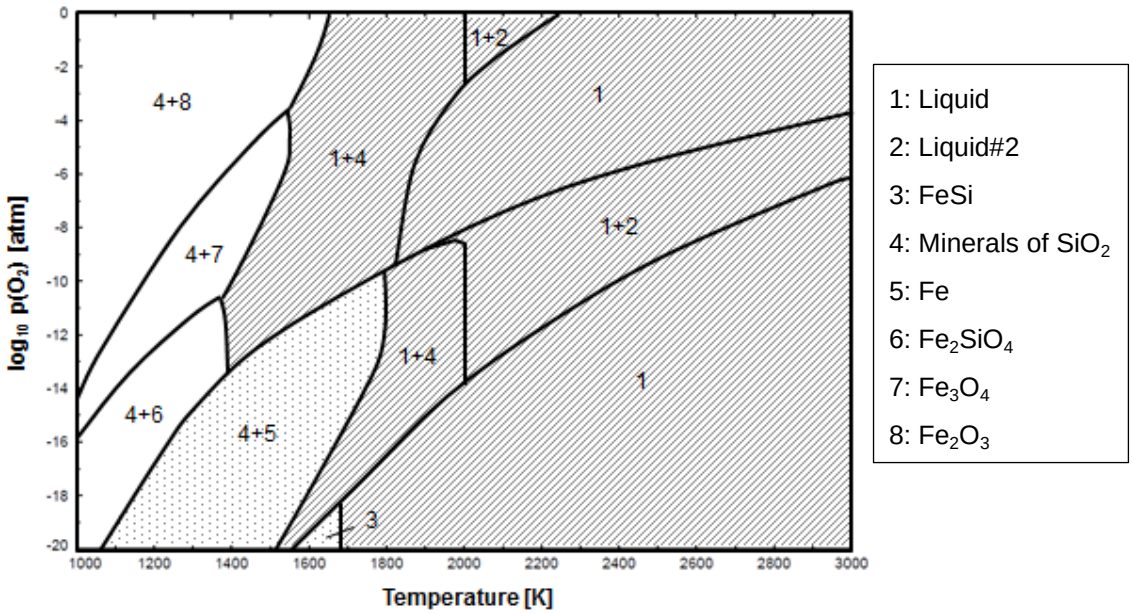

Figure 11 Dependence of the phase-change of Fe–Si on oxygen potential and temperature (Shaded area: liquidus phase or solid-liquid coexistence phase, dotted area: metallic phase or metal-oxide coexistence phase, others: oxide phase)